Check for updates

High-resolution interference microscopy with spectral resolution for the characterization of individual particles and self-assembled meta-atoms

MICHAIL SYMEONIDIS,[1,*] RADIUS N. S. SURYADHARMA,[2] ROSSELLA GRILLO,[3] ANDREAS VETTER,[4] CARSTEN ROCKSTUHL,[2,4] THOMAS BÜRGI,[3] AND TORALF SCHARF[1]

[1]*Nanophotonics and Metrology Laboratory, École Polytechnique Fédérale de Lausanne (EPFL), 1015 Lausanne, Switzerland*
[2]*Institute of Theoretical Solid State Physics (TFP), Karlsruhe Institute of Technology (KIT), Wolfgang-Gaede-Str. 1, 76131 Karlsruhe, Germany*
[3]*Department of Physical Chemistry, University of Geneva, 30 Quai Ernest-Ansermet, 1211 Geneva 4, Switzerland*
[4]*Institute of Nanotechnology (INT), Karlsruhe Institute of Technology, Hermann-von-Helmholtz Platz 1, 76344 Eggenstein-Leopoldshafen, Germany*
[*]*michail.symeonidis@epfl.ch*

Abstract: We apply a high-resolution interference microscope with spectral resolution to investigate the scattering response of isolated meta-atoms in real space. The final meta-atoms consist of core-shell clusters that are fabricated using a bottom-up approach. The meta-atoms are investigated with an increasing complexity. We start by studying silica and gold spheres and conclude with the investigation of the meta-atom, which consists of a silica core sphere onto which gold nanospheres are attached. Numerical simulations entirely verify the measured data. The measuring process involves recording the intensity and phase of the total field emerging from the scattering process of an incident light at the particle in the transmitted half-space with spectral and high spatial resolution. We show that spectrally resolved high-resolution interference microscopy can be used to differentiate between nanoparticles and characterize single meta-atoms, something that is rarely accomplished.

1. Introduction

The concept of materials that possess negative permittivity ϵ and permeability μ was first proposed by Veselago [1], more than forty years ago, and gave birth to the field of meta-materials. Since then, the field has made tremendous progress and has expanded to include any artificially fabricated material whose response can be engineered according to some design. The response is shaped by changing, on a length-scale smaller than the wavelength of operation, the topography of the structure, most of the times consisting of simpler building blocks.

Naturally, the first meta-materials were demonstrated at microwave frequencies [2] and were periodic, non-isotropic structures, fabricated by top-down techniques. The advances in nanofabrication, especially combining different materials, allowed to downscale those structures to operate at optical frequencies [3,4], however the fabrication challenges remain. The techniques used for the fabrication (electron beam lithography, focused ion beam milling) are slow, expensive and limited to planar structures [5,6]. Fabricating real three-dimensional materials with such techniques adds alignment problems and the end results is very sensitive to fabrication errors. What is more, the anisotropy remains, since those structures are essentially stratified media.

Those problems were overcome with the development of bottom-up techniques, based on

chemical engineering or self-assembly methods. Such methods can be used to fabricate real three dimensional, isotropic materials with the trade-off of limited control over the macroscopic arrangement of the final structure [7]. In a strongly diluted scenario, the response of the bulk self-assembled metamaterials can be derived directly from the response of its constituent meta-atoms [8,9]. This means that, by understanding the response of a single meta-atom, the response of the whole three-dimensional metamaterials can be understood. That is the purpose of this contribution. To ease our analysis, we choose an isotropic meta-atom in the form of core-shell cluster meta-atom [10], that consists of a dielectric spherical core, around which plasmonic gold nanoparticles are attached in an isotropic, yet disordered fashion. For the optimization of the fabrication process, the assessment of the structure is necessary, which is mostly done either by imaging the sample or measuring the transmission through a diluted solution.

Frequently used imaging techniques include electron microscopy (SEM, TEM) or near-field microscopy (SNOM). The former techniques reveal the structural integrity of the sample, they cannot capture its optical properties though. The latter ones, although they show the geometry and the optical response of the sample, they tend to be slow and strenuous to carry out. Lastly, characterization through transmittance shows the optical properties, but it cannot link the individual to the collective response. In this work we propose the use of optical interference microscopy to characterize and differentiate between individual meta-atoms and meta-materials. We capture the intensity and phase information of the transmitted field, onto which the optical properties of the sample are imprinted, utilizing a custom-made High Resolution Interference Microscope with spectral resolution [11]. A high magnification objective allows us to study single meta-atoms that are frequently inaccessible. We start by demonstrating the measurement technique using simple dielectric and metallic spheres and then we move on to study the core-shell cluster meta-atom, by comparing the results with simulations and the simple structures.

2. Materials

In this paper, we show a time-efficient and convenient method for a complete characterization of individual meta-atoms. Once this is achieved, the characterization of assemblies of meta-atoms or meta-surfaces in general can follow. For this purpose, we need to record the information contained in the scattered field of such an object. In the following sections, we will describe the samples preparation, the measurement experimental set-up we are using for retrieving the response in intensity and phase regimes, as well as the detailed description of the simulation procedure.

2.1. Sample preparation

As our study cases, we first consider two simple structures, silica microsphere (purchased from microParticles GmbH) with diameter $D = 304$ nm and gold sphere (purchased from Sigma-Aldrich) with diameter $D = 300$ nm. These structures will be followed by a complex one, a core-shell cluster, which is fabricated using a self-assembly method. More specifically, our meta-atom of choice is composed of a silica core of diameter $D = 310$ nm (purchased from Bangs Laboratories Inc.), covered with gold nanoparticles of diameter $D = 20$ nm. Those plasmonic nanoparticles are fabricated according to the conventional Turkevich method [12]. Briefly, in a round bottomed flask, 600 mL of an aqueous solution of Tetrachloroauric (III) acid (0.25 mM) are heated at 120 °C under vigorous magnetic stirring. When the boiling temperature is reached, the gold is reduced by quickly adding 15 mL of aqueous sodium citrate solution (0.03 M). In about 15 min, the solution color slowly turns from yellow to deep red, resulting in the full reduction of the gold salt into isotropic and monodisperse gold nanoparticles. The self-assembly technique benefits from the electrostatic interaction between the constituent materials. For this reason, it is necessary to alter the surface chemistry of the silica microspheres in order to impart a positive charge, thus inducing an electrostatic attraction to the gold nanoparticles, which are negatively

charged, as a result of their fabrication method. To achieve that, 0.5 mL of the microspheres are added to 2 mL of a 5% (v/v) solution of N-[3-(trimethoxysilyl)propyl]ethylenediamine in ethanol and stirred for 30 min. The solution is then centrifuged at 4000 rpm for 10 min to remove the excess of organosilane, which is then replaced by the same volume of ethanol. To produce core-shell clusters, 10 μL of the functionalized silica core sphere solution is added to 40 mL of the gold nanoparticles solution while vigorously agitating. The adsorption of the gold nanoparticles is immediate, as evidenced by the rapid color change from red to blue [13]. All the samples we considered here are deposited on a glass microscope slide using the blade-coating technique, so as to place individual particles well separated from their neighbors [14]. Because of the randomness in the positions of the samples, only a few measurements were carried out on each sample, in order to demonstrate the functionality and working principle of the proposed technique. This also makes it impossible to image the measured samples with non-conventional imaging techniques, such as SEM or AFM. Arranging the samples in a well-defined grid is the next step to ease the measurements and to enable us to match the results to the corresponding sample.

2.2. Spectrally resolved high-resolution interference microscope

The information about the scatterer is encoded in its scattered field, so our purpose is to retrieve the complete information of the total field, which is the intensity and phase. The phase regime is not often investigated directly in experiments, due to the increased complexity of the optical set-up needed for this purpose, compared to recording only the intensity of the total field. Phase is essential, however, in order to capture the full information about the response of the sample for a particular incident field. In our investigation, we employ a high-resolution interference microscopy with spectral resolution. The schematic of the set-up is shown in Fig. 1. The working principle is derived from a Mach-Zehnder interferometer, thus allowing us to record intensity and phase information [15, 16] at the desired wavelengths. The interference between the object arm, that carries the scatterer information, and the reference arm, reveals their phase difference, allowing us to record the effect of the sample on scattered field. In our set-up we use a supercontinuum source (SuperK Fianium, NTK Photonics) and for each measurement, the operating wavelength is selected by the optical variable filter (VARIA, NKT Photonics). An optical delay line, mounted on a precision translation stage (Standa 8MT177-100), is set to the position that minimizes the optical path difference between the object and referential arms. The optical path of each arm varies through different wavelengths because of the dispersion of the microscope objective and other optical elements and their difference must become shorter than the coherence length of the filtered source. A piezo mirror (Mad City Labs, MCL1946) is deployed to vary the optical path length of the referential arm, inducing the different phase shifts that are necessary for the five-steps phase shifting interferometry technique [17, 18] that we use to extract the phase information. An additional piezo stage (MadCityLabs, MSL1945) allows us to precisely run measurements at different distances from the focal plane of the objective, thus creating a volumetric representation of the scattered field. The position of the tube lens, regulated by a precision stage (Standa 8MT177-100), corrects residual wavefront errors of the objective, so that a flat phase profile can be achieved on the CCD camera (Scion Corporation, CFW-1312M). It should be mentioned, that the position of the delay line and the tube lens is irrelevant for the intensity measurements, as the reference arm is blocked and small wavefront errors do not affect the intensity measurement. Finally, to ensure the best aberrations correction and resolution, we use apochromatic high-NA microscope objectives from Leica, such as PL APO, 250x / 0.95.

3. Measurement methods

In this section, we present the principle of the measurement and explain the experimental procedure. The results are extracted after processing the raw data, and those processing steps are also shown here. Finally, we describe the simulations that are compared to the measured data.
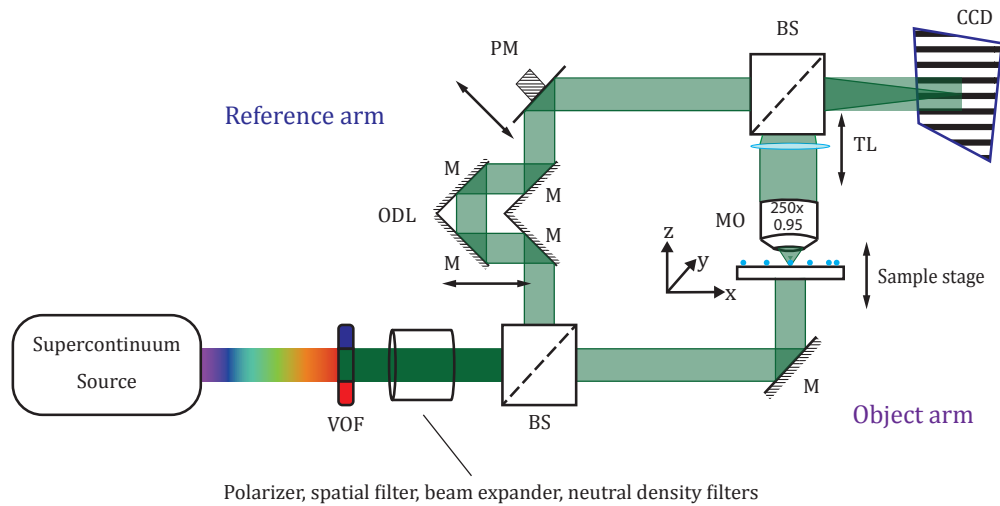
Fig. 1. Schematic diagram of the set-up. The interference microscope is based on the Mach-Zehnder design. VOF: variable optical filter, BS: beam splitter, M: mirror, MO: microscope objective, ODL: optical delay line, PM: piezo-mirror, CCD: charge-coupled device (camera).

3.1. Measurement concept

First, we motivate the measurement procedure by presenting the results acquired for a silica microsphere, that is only the core of the more complex meta-atom. Additionally, we compare the recorded results with simulations to show the validity of the measurement concept. In Figs. 2(a) and 2(c), the recorded intensity and phase are shown. We image the cross-section of each measurement along the center of the sphere in the direction of propagation, since this region is used to characterize the particles. The solid line indicates the value of intensity and phase along the $x = 0\,\mu m$ line. The measurements were generally carried out at four different wavelengths, namely at 450 nm, 500 nm, 600 nm and 700 nm to investigate the spectral response of the samples. In the results shown in Fig. 2 we present results at a wavelength of 450 nm. In panels (b) and (d) of the same figure, the corresponding simulated intensity and phase results are plotted. The simulations will be described further below.

It is clearly seen that both the intensity and the phase are modulated along the central line, which is shown in more detail in Figs. 4 and 5 for intensity and phase data, respectively. There, the spectral dependent response along the $x = 0\,\mu m$ line is shown. As we move the sample along the propagation direction, the relative intensity and the phase difference between the incident and scattered field change, and their interference creates the observed modulation effect [19]. The modulation in intensity is used for volumetric tracking of nanometer-sized biological samples [20] and conventional nano- and microparticles [21]. Although those techniques are holographic measurements in principle, they only utilize the intensity measurements to infer the desired parameters, which has, nevertheless, the benefit of enabling fast time-resolved imaging [22]. In our case, we also record the modulation of the phase of the total field and use the combined information to compare the measured response of the sample, when illuminated by a plane wave, to the simulated response. We study only the static properties of the sample, so we can afford the increased recording time that the phase extraction requires.

The intensity and phase modulation is strongest at the central line, which is the reason why we use it for comparison purposes. The optical properties of the scatterer (absorption and induced phase) are translated into the scattered field, thus each sample creates, in principle, a different
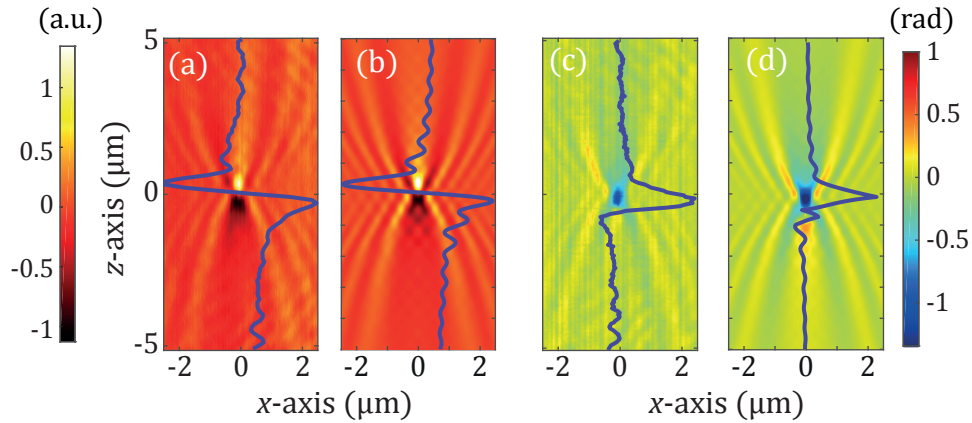
Fig. 2. Measured (left) and simulated (right) results of (a), (b) intensity and (c), (d) phase profile of a silica microsphere of diameter $D = 304$ nm, when illuminated by plane wave at wavelength of $\lambda = 450$ nm. The cross-section is along the x-axis in the middle of the particle and along the propagation direction (z-axis).

profile. In the following we describe the procedure put in place to obtain these results from the measured raw data.

3.2. Data post-processing

The data acquired from our device were first post-processed in order to remove the background and the bias of the measurements. For the intensity data, the process is derived by the *through the focus scanning optical microscopy* (TSOM) technique [23] and can be summarized as follows:

1. Block the reference arm and record several instances (slices) of the intensity profile, as we translate the sample in the z direction.

2. Normalize every slice of the raw data with its mean value.

3. Remove the sample, get a single recording of the background intensity and normalize it as well to its mean value.

4. Subtract the normalized background image from every normalized intensity slice. The final result also contains negative values at some pixel positions where the intensity recorded in the presence of the sample is less than the background intensity. This lower intensity in the presence of the sample is the direct consequence of the destructive interference between the scattered and incident field in some spatial locations.

In the case of the phase recordings, the following steps were taken:

1. Record five interference images and extract the raw phase map using the five-steps phase shifting interferometry technique, as we translate the sample in the z direction.

2. Filter each slice using a $5x5$ averaging window.

3. Unwrap the phase at every slice.

4. Remove the sample, record a single background phase map and filter it using the same averaging window.

5. Unwrap the background phase.

6. Subtract the unwrapped background phase from every slice of the unwrapped recorded phase.

7. Remove any residual tilt and rewrap the phase inside the $[-\pi, \pi)$ interval.

A comparison between the raw and processed data of a gold nanosphere ($D = 300$ nm), illuminated by plane wave at $\lambda = 600$ nm is shown in Fig. 3. The background on the camera, appearing here as vertical lines, is considerably suppressed and the self-correlation of the phase values along the z axis is restored.
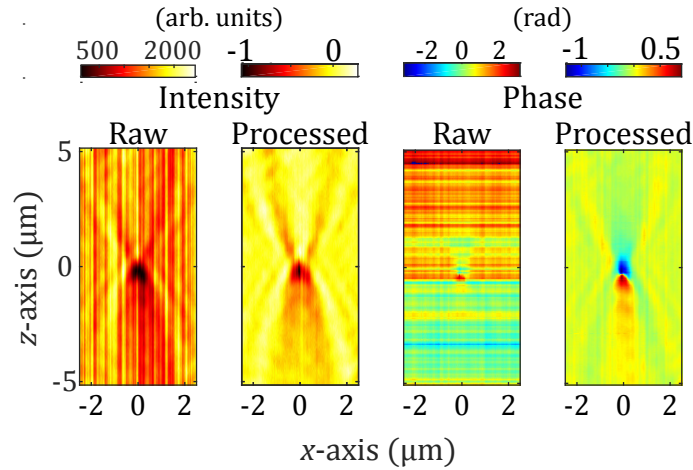
Fig. 3. Comparison between raw and processed data for intensity (left) and phase (right). The sample under study is a gold nanoparticle of diameter $D = 300$ nm, illuminated by a plane wave at $\lambda = 600$ nm. The images show the cross-section in the xz plane through the middle of the particle.

3.3. Simulations

In order to better understand the response of the various structures, we simulate them and also take into account the finite resolution of the measuring system. We implement a plane wave decomposition [24] to have an accurate comparison to the experimental data. The field is obtained by using multiple scattering formalism that solves Maxwell's equations for the pertinent geometry [25].To do this, we consider an x-polarized incident wave, $\mathbf{E}_{inc} = E_{inc}(x, y, z, \lambda)\hat{\mathbf{x}}$. Using this incident field, we calculate the total field at a certain $x - y$ plane at a distance z_0 from the origin of the scatterer, $\mathbf{E}(x, y, z_0, \lambda) = E_x(x, y, z_0, \lambda)\hat{\mathbf{x}} + E_y(x, y, z_0, \lambda)\hat{\mathbf{y}} + E_z(x, y, z_0, \lambda)\hat{\mathbf{z}}$. Due to the fact that the resulted x-component of the scattered field is much larger than the other two components, we only consider this component in the following. After Fourier transforming the field into the reciprocal space $\hat{E}_x(k_x, k_y, z_0, \lambda)$, we suppress all spatial frequencies larger than those accepted by the numerical aperture of our system (NA=0.95). This technique allows us to reproduce the low-pass behavior of our system. The result is the filtered electric field in reciprocal space, $\hat{E}_x(k'_x, k'_y, z_0, \lambda)$, as it is filtered by the microscope objective. Then, we forward and backward propagate this referential field at different z, $\hat{E}_x(k'_x, k'_y, z, \lambda)$. Finally, we transform it back to real space by using inverse Fourier transform and obtain the field at the same z, $E_x(x, y, z, \lambda)$. The intensity profiles are the square of the absolute value of the electric field, from which we subtract the intensity of the incident field, $|E_x|^2 - |E_{inc}|^2$ to ease the

comparison with the measured data. In experiments, we subtract the background image, which translates to the subtraction of the incident field intensity. The phase value is the unwrapped phase difference between the phases of the x component of the total field and the incident field $Unwrap\{\angle E_x - \angle E_{inc}\}$, which is analog to the data post-processing procedure. In our set-up, the phase accumulated by y- and z-components will not contribute to the signal, as they only appear as the background intensity because the reference field is polarized in x-direction. The phase unwrapping based on weighted (simulations) and unweighted (measurements) least-square method was used [26]. For the remainder of this work, we will use the terms *intensity* and *phase* to describe the modified values we get after processing the data as described in this section.

4. Results

In this section, we present and compare the experimental and simulated results obtained for the various samples at the chosen wavelengths. The intensity plots have been normalized to the absolute value of the global maximum of each set of lines. As a general remark, the agreement between simulation and measurement is satisfying, especially for the form of the profiles. The disagreement between the values and the contrast (difference between minimum and maximum value) can be explained by a number of reasons. Firstly, the bandwidth of the source, although limited ($BW \approx 10\,$nm), is still wider than that considered in the simulations (that is essentially strictly monochromatic), so very sharp resonant effects captured in the simulation are smoothed out in the measurement. Additionally, aberrations are always present in the measurements, so we cannot capture a perfect representation of the measured field. This leads to a decreased contrast in the measured results. Finally, we are looking for small variations in a strong background, so noise also impacts the final results. We do not consider variations from the nominal shape (spherical) and size as a reasons for creating discrepancies between simulation and experiment, since any small variation produces unlikely any observable effect. There will be differences in the multipolar composition but this is unlikely to be drastic. It should be stressed, that, since the size of the examined particles is smaller than the resolution of the imaging system, we do not use the interferometric microscope to image the samples themselves, but rather to collect the scattered light and the illumination field.

4.1. Silica sphere

We will begin with the results obtained from a silica sphere of diameter $D = 304\,$nm. In Figs. 4(a) and 4(b), the intensity profiles for simulated and recorded data are shown. The profiles in both cases are the same, namely a dip before the position of the particle, followed by a peak just after it, which is the result of the focusing caused by the silica sphere. The focused intensity becomes weaker as the wavelength increases, but it always occurs at the same position. Finally, we note that the dip is not as pronounced as the peak.

The results for the simulated and recorded phase are shown in Figs. 5(a) and 5(b), respectively. At the positions where the scattered field has significant power, a retardation (or phase shift) of the total field is observed. As the particle moves away from the focus, the scattered field becomes negligible, and the phase of the total field effectively is that of the incident field. The accumulated phase shift is reduced for longer wavelengths, which can be attributed to the smaller optical path (longer wavevector) inside the sphere. The maximum recorded phase retardation is $\phi \approx -0.4\pi$ for $\lambda = 450\,$nm and the maximum simulated phase shift is $\phi \approx -0.5\pi$ for the same wavelength. As a general remark, the phase profiles are smooth for the dielectric sphere and the intensity profiles always show a focusing effect. We should note here that the profile for $\lambda = 700\,$nm is not centered, which is the result of a mechanical displacement during the measurement.
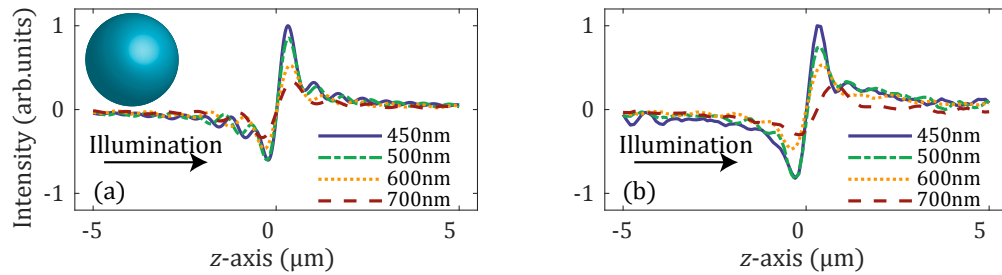
Fig. 4. On-axis values of the (a) simulated and (b) measured intensity profiles of the silica microsphere. The results are in good agreement. The peak after the particle is due to focusing, which occurs at the same position for all wavelengths, but decreases in strength as the wavelength increases.
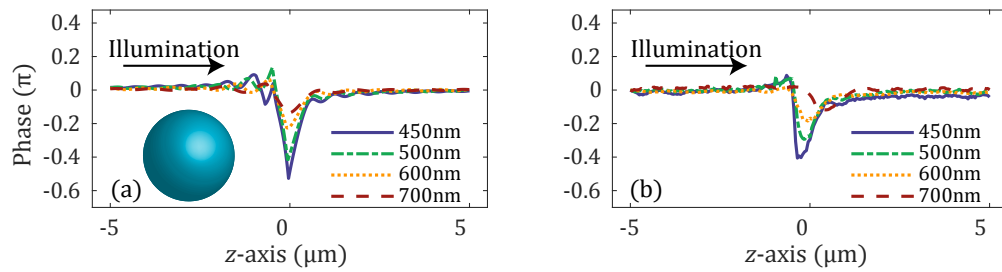

Fig. 5. On-axis values of the (a) simulated and (b) measured phase profiles of the silica microsphere. The profiles in both cases are similar, a pronounced phase change at the particle's position. The maximum measured phase shift is -0.4π, while the maximum calculated is -0.5π, a reasonable difference between simulation and experiment. For the dielectric case, the phase profiles are smooth.

4.2. Gold sphere

We continue with the intensity results from a gold sphere with diameter $D = 300$ nm, that are shown in Figs. 6(a) and 6(b) for simulation and measurement respectively. We use this particle to demonstrate that the measurement is valid for metals as well and to identify the response of a plasmonic structure. In this case, the asymmetry of the experimental data is more pronounced, still, it can be explained by the argumentation at the start of the section and does not invalidate the good agreement with the simulation. The main feature of the metallic sphere is the strong dip at the particle's position, which arises from absorption, and the absence of the focusing effect due to the same reason.

The simulated and measured phase values of the gold nanosphere are shown in Figs. 7(a) and 7(b) respectively. Again, the agreement is quite good, showing a peak and a dip for both cases and an abrupt phase change. The profiles are different compared to the dielectric measurements, which confirms that the scattering cross-section of the particle changes the results and the central profile can be used for benchmarking. There is a spectral dependency that is, nevertheless, rather weak. This is quite reasonable considering the large size of the object and the absorptive nature of the material from which it is made. It is a strongly dissipative system that smoothens out tremendously a possible spectrally narrow response.
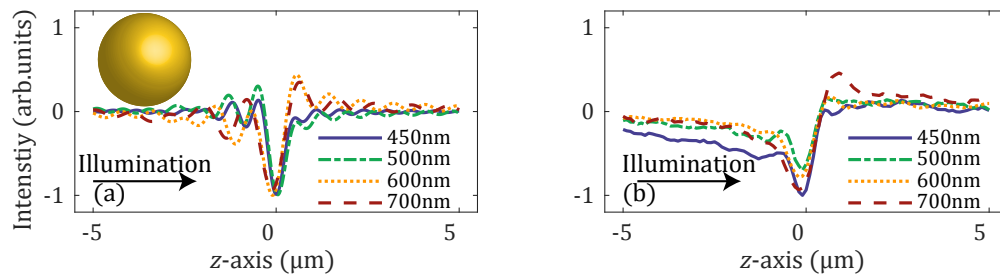
Fig. 6. On-axis values of the (a) simulated and (b) measured intensity profiles of the gold sphere. The profiles are in satisfying agreement. The main features are the dip at the particle's position and the absence of focusing effect that are the result of the metallic nature of the particle. This is in contrast to the results obtained for the dielectric sphere.
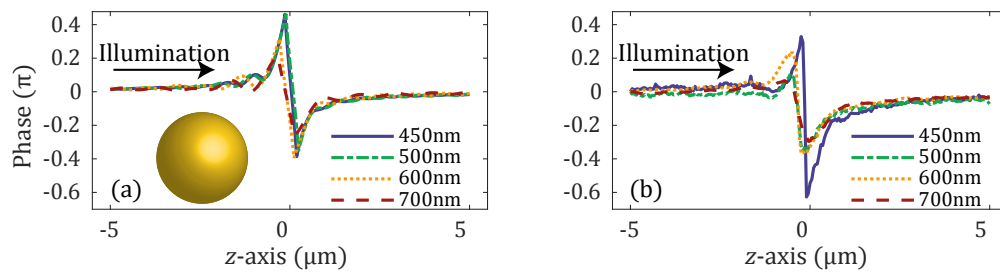

Fig. 7. On-axis values of the (a) simulated and (b) measured phase profiles of the gold sphere. The agreement between the profiles is satisfactory, both showing a peak, immediately followed by a dip and an abrupt phase change between them. These sudden changes are in contrast to the dielectric case.

4.3. Meta-atom

After using two simple structures, in this section we will finally show the results for the core-shell cluster meta-atom. In Figs. 8(a) and 8(b) the simulated and experimental intensity profiles are shown respectively, which bear greater resemblance to the dielectric case compared to the metallic one. The profile with the dip and peak just before and after the particle is retained, although the focusing effect deteriorates faster. The simulated results show a different trend compared to those in Fig. 4(a), since the peak position moves for different wavelengths; the focusing effect is still comparable and more pronounced than that of the measurements. The recorded data follow the same trends as those in Fig. 4(b), only with broader and shallower peaks, that can be attributed to the additional losses introduced by the gold.

The phase results for the same meta-atom are shown in Figs. 9(a) and 9(b) for simulation and measurement respectively. They resemble the response of the silica case more than the gold sphere, with a pronounced phase change at the position of the particle. Comparing Figs. 5(b) and 9(b), we notice that in the first case the accumulated phase is reduced gradually, while in the latter figure there is a sudden drop of the phase accumulation for illuminating wavelength $\lambda > 500$ nm. This difference is due to the effect of the gold nanoparticles around the dielectric core.

From the simulated data, we observe that the meta-atom still has a focusing effect, although the focal spot position changes, and that the accumulated phase is comparable to the simulated silica microsphere case. The experimental data though show a significantly less pronounced focusing effect and less phase accumulation compared to silica measurements. Consequently, we can observe the effect of the gold nanoparticles. However, there is an excess of them, due to
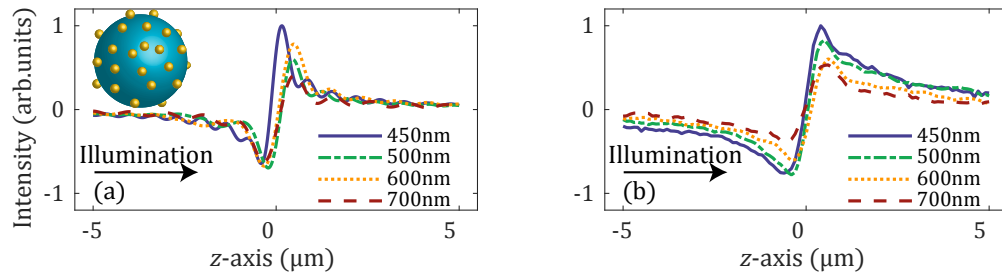
Fig. 8. On-axis values of the (a) simulated and (b) measured intensity profiles of the core-shell cluster meta-atom. The profiles resemble strong those of the silica nanosphere, although the position and the intensity of the focus are not the same.
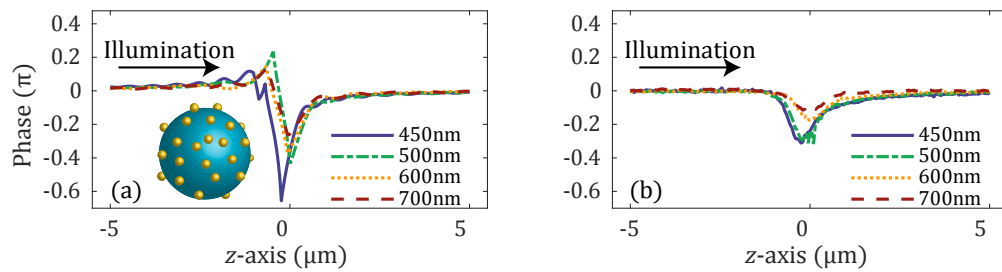

Fig. 9. On-axis values of the (a) simulated and (b) measured phase profiles of the core-shell cluster meta-atom. The profiles resemble strong those of the silica nanosphere, showing a pronounced phase change at the particle's position. However, the wavelength at which the phase accumulation changes more is different, showing the effect of the gold nanoparticles.

the fabrication and deposition process, which create a layer and alters the results. The excessive gold nanoparticles have a greater influence than those on the dielectric core. This can be seen in Figs. 10(a) - 10(c), which show scanning electron microscopy images of the samples. It is shown that less gold nanoparticles attach on the surface of the silica core when compared to the gold nanoparticles lying around it.
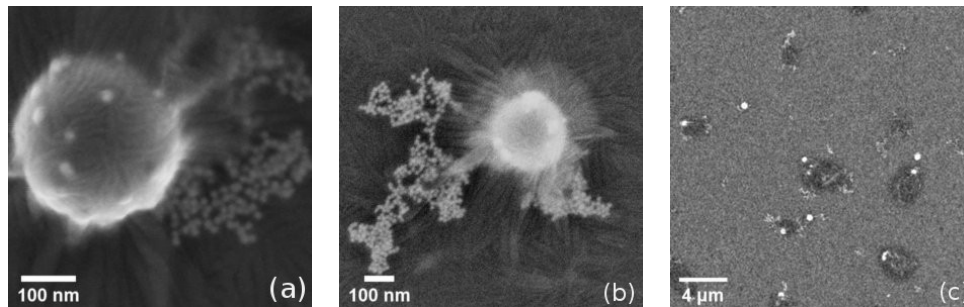

Fig. 10. Scanning electron microscopy images of the sample. (a),(b): Dielectric core with gold nanoparticles attached to it and excessive nanoparticles around. (c): Larger overview showing individual dielectric cores (bright spots), with the excess of gold nanoparticles clearly visible.

Under optical microscopy in reflection configuration, the sample is imaged as shown in

Figs. 11(a) - 11(c), where brightfield, darkfield, and defocused darkfield images of the sample are shown, respectively. Again, we notice a large particle with many more, smaller particles in close proximity. The scattering of the larger particle is dominant, since it is much brighter in the darkfield imaging, even when it is out of focus.
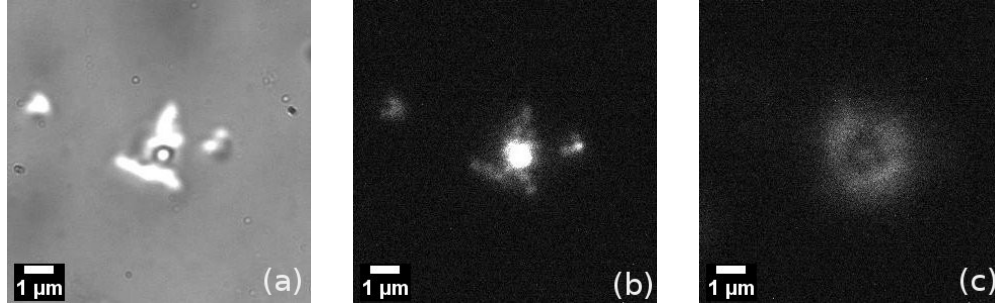

Fig. 11. Reflection microscopy. (a) Brightfield, (b) darkfield and (c) defocused darkfield images of a core-shell cluster meta-atom. The excessive gold nanoparticles around the dielectric core that dominates the response are shown. The defocused image shows that the core is indeed a silica sphere.

5. Experimental results comparison

In the last part, we compare only the experimental data between the different particles for illuminating wavelengths of 450 nm, 500 nm and 600 nm, in order to demonstrate the flexibility of the set-up. The results are shown in Figs. 12 - 14 for 450 nm to 600 nm, respectively. In all figures, panel (a) includes the intensity measurements, while panel (b) shows the phase regime.

In the previous section it was concluded that the meta-atom acts more like a silica sphere, since the profiles agree better with the silica case and the total response is dominated by the core. The extinction cross-section of the silica core is in the range from $C_{ext} \approx 5 \times 10^4 \, \text{nm}^2$ to $12 \times 10^4 \, \text{nm}^2$ and is purely due to scattering, while the maximum extinction cross-section of the gold nanoparticles of $D = 20 \, \text{nm}$ is $C_{ext}^{max} \approx 130 \, \text{nm}^2$ and is dominated by absorption. Figure 12 shows that at $\lambda = 450 \, \text{nm}$, the dielectric and metallic particles are distinguishable either from the intensity or the phase profiles.
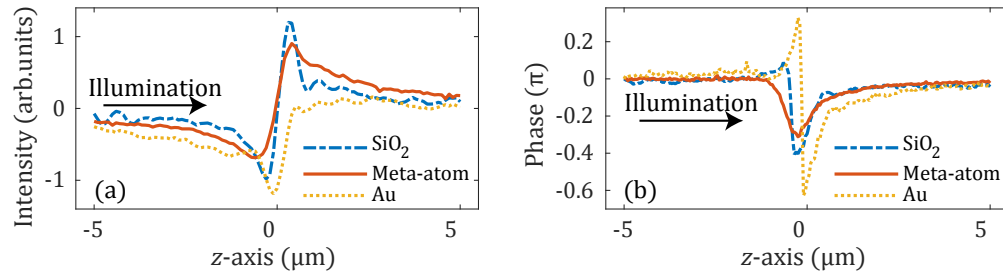

Fig. 12. Measured on-axis (a) intensity and (b) phase values of silica microsphere (SiO$_2$), core-shell cluster structure (Meta-atom) and gold sphere (Au). The illumination wavelength is $\lambda = 450 \, \text{nm}$. The meta-atom profile resembles strongly the silica sphere. The metallic particle can be distinguished both in intensity and phase measurements.

The phase retardation of the silica sphere is reduced when moving from $\lambda = 450 \, \text{nm}$ to $500 \, \text{nm}$, while it remains constant for the meta-atom. This can be attributed to the presence of the small

gold nanospheres that possess a resonance around $\lambda = 500\,\text{nm}$ that can be shifted due to size variations and aggregation of excess particles [27]. From Fig. 13 we see that the metallic particle is easier distinguishable in the intensity regime.
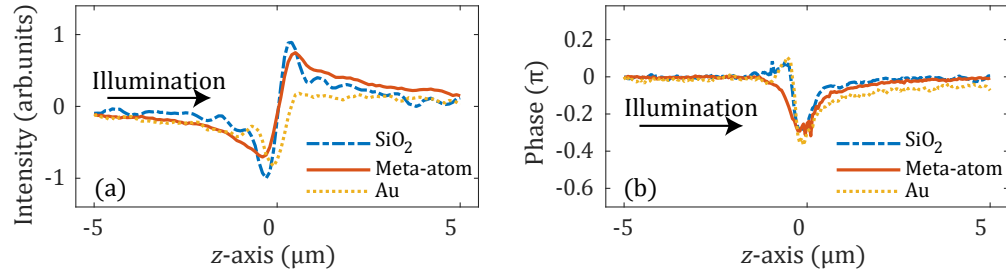

Fig. 13. Measured on-axis (a) intensity and (b) phase values of silica microsphere (SiO_2), core-shell cluster structure (Meta-atom) and gold sphere (Au). The illumination wavelength is $\lambda = 500\,\text{nm}$. The dielectric sphere has accumulated less phase compared to the previous measurement (Fig. 12), while the meta-atom the same, due to the presence of the gold nanoparticles. In this case, the metallic sphere can be easier distinguished in the intensity regime.

Lastly, at longer wavelengths the scattering cross-section of the small particles is further reduced and both the silica sphere and the meta-atom follow the same trends and become indistinguishable. It is interesting to notice though, as shown in Fig. 14, the intensity profile of the metallic particle resembles strongly the dielectric case, and now the distinction of the particles is easier in the phase regime. Those examples show that recording the intensity and phase information at different wavelengths gives a more complete representation of the nature of the sample under study and its response.
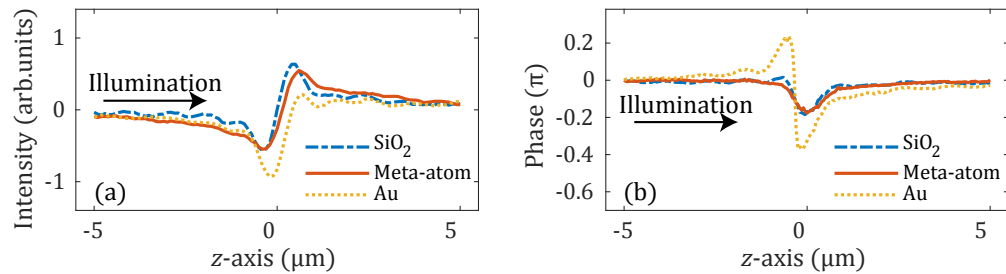

Fig. 14. Measured on-axis (a) intensity and (b) phase values of silica microsphere (SiO_2), core-shell cluster structure (Meta-atom) and gold sphere (Au). The illumination wavelength is $\lambda = 600\,\text{nm}$. The meta-atom and the silica sphere have almost identical responses, due to the small scattering cross-section of the gold nanoparticles. The intensity response of the gold sphere bears strong resemblance to the silica case, but the profiles in phase are easily distinguishable.

6. Conclusions

We summarize the presented work on characterizing individual nanoscatterers by restating the key points. First, we investigated simple gold and silica spheres, by recording the intensity and phase of the light transmitted through the samples. The shape of the profile along the propagation axis and through the center of the particle was used to differentiate them. Accordingly, the same

profiles were extracted for a core-shell cluster meta-atom with a silica core and gold nanospheres attached on it. By comparing the results, we were able to identify the dominant components and the effect of the constituent parts. The results were verified using numerical simulations that agreed well with the measurements. In the end, we demonstrated that this technique can be used for single meta-atoms and, consequently, complex structures characterization, by recording its complete response at different wavelengths. It can also be used to differentiate between distinct particles with similar dimensions. The results presented here show that the experimentally recorded phase and intensity from a single meta-atom can reveal its optical properties and, by comparison to simulated data, assess its structure and performance. With this, we provide impetus for experimental investigation of the response of a broad range of meta-atoms. The next step is to expand this technique to an ensemble of meta-atoms which form meta-surfaces or bulk three dimensional meta-materials. Furthermore, a correlation between the structures, the measured profiles and the simulated features can be established, in order to create a mapping of the possible geometries that have a specific optical response.

References

1. V. Veselago, "The electrodynamics of substances with simultaneously negative values of epsilon and mu," Sov. Phys. Uspekhi **10**, 509–514 (1968).
2. I. B. Vendik and O. G. Vendik, "Metamaterials and their application in microwaves: A review," Tech. Phys. **58**, 1–24 (2013).
3. S. Linden, C. Enkrich, M. Wegener, J. Zhou, T. Koschny, and C. M. Soukoulis, "Magnetic Response of Metamaterials at 100 Terahertz," Science **306**, 1351 (2004).
4. C. Enkrich, M. Wegener, S. Linden, S. Burger, L. Zschiedrich, F. Schmidt, J. F. Zhou, T. Koschny, and C. M. Soukoulis, "Magnetic Metamaterials at Telecommunication and Visible Frequencies," Phys. Rev. Lett. **95**, 203901 (2005).
5. C. M. Soukoulis and M. Wegener, "Past achievements and future challenges in the development of three-dimensional photonic metamaterials," Nat. Photonics (2011).
6. H. Moser and C. Rockstuhl, "3d THz metamaterials from micro/nanomanufacturing," Laser Photonics Rev. **6**, 219–244 (2012).
7. S. Mühlig, A. Cunningham, J. Dintinger, T. Scharf, T. Bürgi, F. Lederer, and C. Rockstuhl, "Self-assembled plasmonic metamaterials," Nanophotonics **2** (2013).
8. A. Kuzyk, R. Schreiber, Z. Fan, G. Pardatscher, E.-M. Roller, A. Högele, F. C. Simmel, A. O. Govorov, and T. Liedl, "DNA-based self-assembly of chiral plasmonic nanostructures with tailored optical response," Nature **483**, 311 (2012).
9. N. R. Suryadharma and C. Rockstuhl, "Predicting Observable Quantities of Self-Assembled Metamaterials from the T-Matrix of Its Constituting Meta-Atom," Materials **11** (2018).
10. J. Dintinger, S. Mühlig, C. Rockstuhl, and T. Scharf, "A bottom-up approach to fabricate optical metamaterials by self-assembled metallic nanoparticles," Opt. Mater. Express **2**, 269–278 (2012).
11. C. Rockstuhl, I. Marki, T. Scharf, M. Salt, H. Peter Herzig, and R. Dändliker, "High resolution interference microscopy: a tool for probing optical waves in the far-field on a nanometric length scale," Curr. Nanosci. **2**, 337–350 (2006).

12. J. Kimling, M. Maier, B. Okenve, V. Kotaidis, H. Ballot, and A. Plech, "Turkevich Method for Gold Nanoparticle Synthesis Revisited," The J. Phys. Chem. B **110**, 15700–15707 (2006).
13. S. Mühlig, A. Cunningham, S. Scheeler, C. Pacholski, T. Bürgi, C. Rockstuhl, and F. Lederer, "Self-Assembled Plasmonic Core-Shell Clusters with an Isotropic Magnetic Dipole Response in the Visible Range," ACS Nano **5**, 6586–6592 (2011).
14. H. Yang and P. Jiang, "Large-Scale Colloidal Self-Assembly by Doctor Blade Coating," Langmuir **26**, 13173–13182 (2010).
15. M.-S. Kim, T. Scharf, S. Mühlig, C. Rockstuhl, and H. P. Herzig, "Engineering photonic nanojets," Opt. express **19**, 10206–10220 (2011).
16. M.-S. Kim, T. Scharf, S. Mühlig, C. Rockstuhl, and H. P. Herzig, "Gouy phase anomaly in photonic nanojets," Appl. Phys. Lett. **98**, 191114 (2011).
17. E. P. Goodwin and J. C. Wyant, *Field Guide to Interferometric Optical Testing*, SPIE Field Guides (SPIE, 2006).
18. P. Hariharan, B. F. Oreb, and T. Eiju, "Digital phase-shifting interferometry: a simple error-compensating phase calculation algorithm," Appl. Opt. **26**, 2504–2506 (1987).
19. J. Hwang and W. Moerner, "Interferometry of a single nanoparticle using the Gouy phase of a focused laser beam," Opt. Commun. **280**, 487–491 (2007).
20. P. Kukura, H. Ewers, C. Müller, A. Renn, A. Helenius, and V. Sandoghdar, "High-speed nanoscopic tracking of the position and orientation of a single virus," Nat. Methods **6**, 923 (2009).
21. F. C. Cheong, B. J. Krishnatreya, and D. G. Grier, "Strategies for three-dimensional particle tracking with holographic video microscopy," Opt. Express **18**, 13563–13573 (2010).
22. Y.-F. Huang, G.-Y. Zhuo, C.-Y. Chou, C.-H. Lin, W. Chang, and C.-L. Hsieh, "Coherent Brightfield Microscopy Provides the Spatiotemporal Resolution To Study Early Stage Viral Infection in Live Cells," ACS Nano **11**, 2575–2585 (2017).
23. R. K. Attota and H. Kang, "Parameter optimization for through-focus scanning optical microscopy," Opt. Express **24**, 14915–14924 (2016).
24. J. W. Goodman, *Introduction to Fourier Optics*, McGraw - Hill Series in Electrical and Computer Engineering (McGraw - Hill, 1996), 2nd ed.
25. Y.-l. Xu, "Electromagnetic scattering by an aggregate of spheres," Appl. Opt. **34**, 4573–4588 (1995).
26. D. C. Ghiglia and L. A. Romero, "Robust two-dimensional weighted and unweighted phase unwrapping that uses fast transforms and iterative methods," J. Opt. Soc. Am. A **11**, 107–117 (1994).
27. V. Myroshnychenko, J. Rodríguez-Fernández, I. Pastoriza-Santos, A. M. Funston, C. Novo, P. Mulvaney, L. M. Liz-Marzán, and F. J. García de Abajo, "Modelling the optical response of gold nanoparticles," Chem. Soc. Rev. **37**, 1792–1805 (2008).